Peptide-Directed Assembly of Single-Helical Gold Nanoparticle Superstructures Exhibiting Intense Chiroptical Activity

Andrea D. Merg,[†] Jennifer C. Boatz,[‡] Abhishek Mandal,[‡] Gongpu Zhao,[‡] Soumitra Mokashi-Punekar,[†] Chong Liu,[†] Xianting Wang,[‡] Peijun Zhang,[‡] Patrick C. A. van der Wel,*[‡] and Nathaniel L. Rosi*[†]

[†]Department of Chemistry, University of Pittsburgh, 219 Parkman Avenue, Pittsburgh, Pennsylvania 15260, United States
[‡]Department of Structural Biology, School of Medicine, University of Pittsburgh, 3501 Fifth Avenue, Pittsburgh, Pennsylvania 15260, United States

  Supporting Information

ABSTRACT: Chiral nanoparticle assemblies are an interesting class of materials whose chiroptical properties make them attractive for a variety of applications. Here, C_{18}-$(PEP_{Au}^{M-ox})_2$ (PEP_{Au}^{M-ox} = AYSSGAPPM^{ox}PPF) is shown to direct the assembly of single-helical gold nanoparticle superstructures that exhibit exceptionally strong chiroptical activity at the plasmon frequency with absolute g-factor values up to 0.04. Transmission electron microscopy (TEM) and cryogenic electron tomography (cryo-ET) results indicate that the single helices have a periodic pitch of approximately 100 nm and consist of oblong gold nanoparticles. The morphology and assembled structure of C_{18}-$(PEP_{Au}^{M-ox})_2$ are studied using TEM, atomic force microscopy (AFM), Fourier transform infrared (FTIR) spectroscopy, circular dichroism (CD) spectroscopy, X-ray diffraction (XRD), and solid-state nuclear magnetic resonance (ssNMR) spectroscopy. TEM and AFM reveal that C_{18}-$(PEP_{Au}^{M-ox})_2$ assembles into linear amyloid-like 1D helical ribbons having structural parameters that correlate to those of the single-helical gold nanoparticle superstructures. FTIR, CD, XRD, and ssNMR indicate the presence of cross-β and polyproline II secondary structures. A molecular assembly model is presented that takes into account all experimental observations and that supports the single-helical nanoparticle assembly architecture. This model provides the basis for the design of future nanoparticle assemblies having programmable structures and properties.
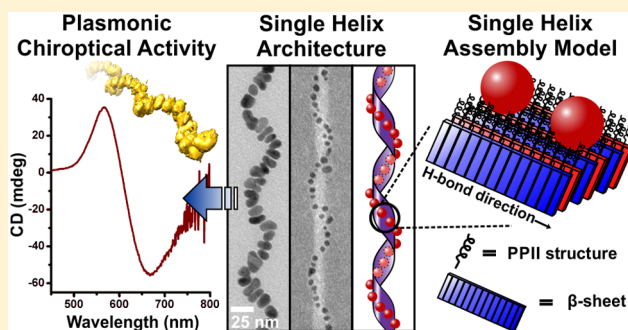
INTRODUCTION

Chiral nanoparticle assemblies are an emerging class of materials.[1−17] They have the potential to serve as nanoscale circular polarizers[18,19] and chiroptical sensors,[20−22] and they represent an interesting new entry into the metamaterials catalogue.[18,19,23] Peptides, which can assemble into chiral architectures, are attractive molecular building blocks that can be used to direct the assembly of nanoparticles into chiral superstructures.[24−28] We have developed peptide-based nanoparticle assembly methods, where tailored peptide conjugate molecules are used to direct the assembly of nanoparticles.[26−35] We have used these methods to assemble gold nanoparticles into double-helical arrays having tailorable structures and chiroptical properties.[26,27,29] Gold-binding peptide conjugate molecules, R-PEP_{Au} (R = organic tail; PEP_{Au} = AYSSGA-PPMPPF[36,37]), play a dual role in this methodology: they bind to gold nanoparticle surfaces during particle synthesis and they direct particle assembly. While significant progress has been made toward (i) understanding how AYSSGAPPMPPF associates with gold nanoparticle surfaces[37−42] and (ii) understanding how both R-groups and intrinsic secondary structure influence R-PEP_{Au} assembly,[26,28,32] we have yet to establish a molecular-level understanding that accounts for the

dual role that R-PEP_{Au} conjugates play in the context of constructing nanoparticle superstructures. Significant questions remain unanswered: How does AYSSGAPPMPPF associate to nanoparticles within an assembled nanoparticle superstructure? How do R-AYSSGAPPMPPF conjugates pack and assemble within a nanoparticle superstructure? How do these conjugates simultaneously self-assemble *and* bind to gold nanoparticle surfaces? Uncovering answers to these questions is paramount to advancing peptide-based methods for assembling nanoparticle superstructures.

Here, we report the preparation of unique gold nanoparticle single helices that exhibit exceptionally strong plasmonic chiroptical activity. Motivated by these results, we rigorously examine the underlying molecular basis of these superstructures and ultimately arrive at a structural model that thoroughly accounts for their assembly. Through these studies, we make considerable progress toward answering the fundamental questions listed above, and we ultimately arrive at a new understanding of this methodology that will motivate future
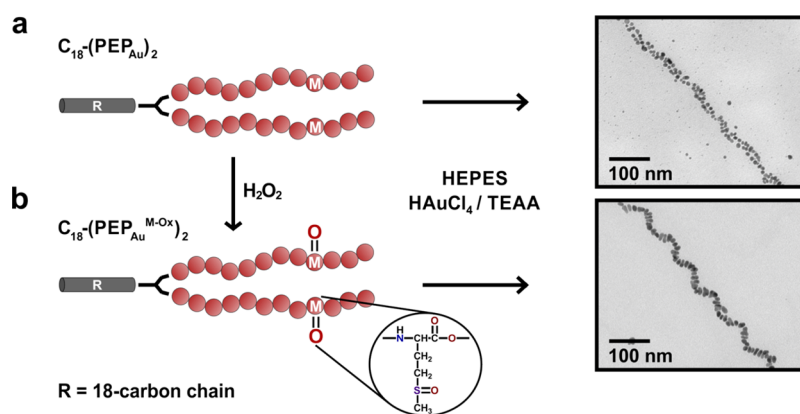
Figure 1. Preparation of (a) double- and (b) single-helical nanoparticle superstructures from C_{18}-$(PEP_{Au})_2$ and C_{18}-$(PEP_{Au}^{M-ox})_2$, respectively, under identical reaction conditions. C_{18}-$(PEP_{Au}^{M-ox})_2$ was prepared via oxidation using H_2O_2.

peptide design strategies for the rational construction and optimization of chiral nanoparticle superstructures.

RESULTS AND DISCUSSION

Single Helix Synthesis and Chiroptical Properties. We recently reported that the divalent peptide conjugate C_{18}-$(PEP_{Au})_2$ (Figure S1a) directs the assembly of double-helical gold nanoparticle superstructures when mixed with gold salts, assembly buffers, and reducing agents (Figure 1a).[28] In subsequent studies, single-helical gold nanoparticle super-structures, rather than double helices, were, at times, observed as the sole product. These confounding results prompted us to investigate the origin of the single helix architecture. Since the synthetic procedures used to prepare the double and single helices were virtually indistinguishable (e.g., identical gold salt, identical buffer, and identical reagent concentrations), we carefully characterized the C_{18}-$(PEP_{Au})_2$ used in each synthesis, reasoning that a small impurity or chemical change to the conjugate may have led to the observed results. High-resolution liquid chromatography mass spectrometry (HR-LCMS) revealed that the molecular weight of the conjugates that directed the formation of the single helices was 16 m/z larger than expected ($z = 2$), corresponding to a 32 au increase in the molecular weight. The thioether functional group of methionine can undergo oxidation to the sulfoxide;[43] a 16 m/z increase would result if both methionine residues of C_{18}-$(PEP_{Au})_2$ were oxidized (Figure S1b). Therefore, we hypothesized that oxidation of C_{18}-$(PEP_{Au})_2$ to C_{18}-$(PEP_{Au}^{M-ox})_2$ (PEP_{Au}^{M-ox} = AYSSGAPPM^{ox}PPF) results in the formation of single-helical superstructures. To test this hypothesis, we chemically oxidized C_{18}-$(PEP_{Au})_2$; LCMS data for these oxidized conjugates confirmed the increase in molecular weight associated with the addition of two oxygens (Figure S2). The oxidized conjugates exclusively directed the assembly of single-helical gold nanoparticle superstructures (Figure 1b).

We next characterized the single-helical gold nanoparticle assemblies. Transmission electron microscopy (TEM) images (Figures 2a−c and S3) reveal that the single helices have an average pitch of 94.4 ± 6.6 nm (Figure 2d) and are composed of individual rod-like nanoparticles with lengths of 16.6 ± 3.0 nm and widths of 9.6 ± 1.9 nm (Figure S4). At the early stages of the synthesis and assembly process, the nanoparticles are spherical and bound to the 1D C_{18}-$(PEP_{Au}^{M-ox})_2$-based fibers (Figures 2c and S5), but over time they grow into oblong rod-like nanoparticles (Figure S5). Throughout the nanoparticle
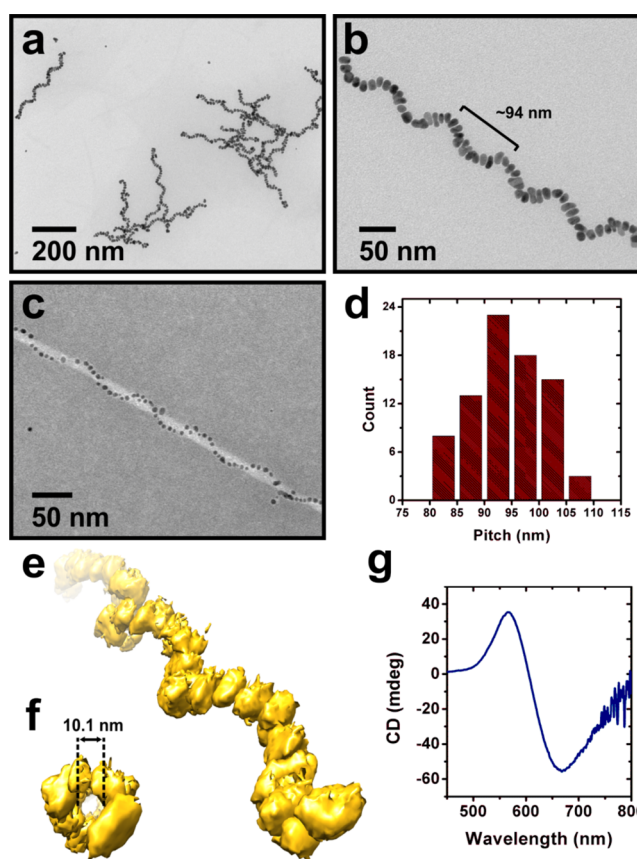

Figure 2. Single helix characterization. (a, b) TEM images of single-helical gold nanoparticle superstructures after 15 h of reaction and (c) negative-stained TEM image after 30 min of reaction. (d) Pitch of the helices, measured from TEM (94.4 ± 6.6 nm; based on 80 counts). The cryo-ET 3D reconstruction of the single helices reveals their (e) left-handed helicity and, when viewed along the helix axis, their (f) core diameter where the fiber resides. (g) CD spectrum of the single-helical superstructures.

growth process, the nanoparticles remain bound to the fibers (Figure S5). These observations are consistent with our previously reported studies.[26,30] We note that, in this method, *in situ* nanoparticle growth in the presence of the peptide conjugates is required to achieve ordered nanoparticle assemblies.[26] Cryogenic electron tomography (cryo-ET) was employed to determine the 3D architecture of the single helices

(Figure 2e,f). The reconstructed tomographic volume confirms that the helices are left-handed, which can be attributed to L amino acid residues comprising the peptides.[27] Structural parameters were also gathered from the 3D reconstruction of the helices. The pitch is 102.0 ± 2.5 nm, within error of the measured data from 2D TEM images, and the rotation angle per particle is 34.3 ± 4.9°, corresponding to approximately 10–11 nanoparticles per pitch length (Figure S6a,b). The inner diameter of the helical superstructure is 10.1 ± 0.6 nm (Figures 2e and S6c). This distance corresponds to the measured width of the fibers (*vide infra*).

Circular dichroism (CD) spectroscopy was used to characterize the chiroptical activity of the single helices. The single helices exhibit a strong bisignate peak centered at approximately 600 nm, near the collective plasmonic extinction band for the assemblies (Figure 2g). Others have reported a visible plasmonic CD peak for peptide-capped gold nanoparticles.[44] However, gold nanoparticles capped with PEP_{Au}^{M-ox} showed only a weak CD signal (Figure S7). Therefore, we can reasonably conclude that the strong plasmonic CD signal for the single helices originates from the chiral helical arrangement of gold particles; indeed, the observed signal is consistent with previous theoretical predictions.[1,27] It is important to compare the chiroptical activity of the single helices to other reported chiral nanoparticle assemblies. The anisotropy factor, *g*, is typically used as a benchmark value for determining the intensity of the chiroptical signal. Optimized assemblies (Figure S8a,b), for which synthetic conditions were tuned to increase particle dimensions, have an absolute *g*-factor up to ∼0.04 (Figure S8e), which, to our knowledge, is one of the highest reported to date for comparable nanoparticle assemblies.[9,13,14,45]

Peptide Conjugate Assembly Studies. The intense chiroptical activity of single helices prompted us to examine the assembly and structure of C_{18}-$(PEP_{Au}^{M-ox})_2$. Understanding the underlying molecular structure of the fibers and how it correlates to the final nanoparticle assembly will allow for rational design of peptide conjugate building blocks and precise control over nanoparticle superstructure assembly and properties.

We first studied the morphology of the C_{18}-$(PEP_{Au}^{M-ox})_2$ fibers in the absence of gold nanoparticles. Acylated peptide amphiphiles are known to assemble into two principal helical morphologies: twisted and helical ribbons (Figure 3a,b).[46–52] Both assemblies are defined by a cross-β amyloid-like structure. Twisted ribbons are characterized by their saddle-like curvature with a C2 symmetry axis, and both ribbon faces are equally exposed. Helical ribbons, on the other hand, have cylindrical curvature, and one face of the ribbon is directed toward the interior of the helical coil and the other is directed to the exterior. In both cases, the helicity originates from the chirality of the peptide-based molecular building blocks.[53] The observed single helix architecture suggests that C_{18}-$(PEP_{Au}^{M-ox})_2$ fibers assemble into helical ribbons and the gold nanoparticles decorate the exterior face of the helical ribbon. Evidence from previous studies suggests that the twisted ribbon morphology favors the formation of a double-helical nanoparticle superstructure, where the particles associate to either both edges or both faces of the ribbon.[26,28]

To precisely determine the fiber morphology, samples were analyzed using numerous microscopy techniques. TEM verifies the presence of 1D fibers (Figure 3c), in addition to small pseudospherical aggregates, which are always present in varying
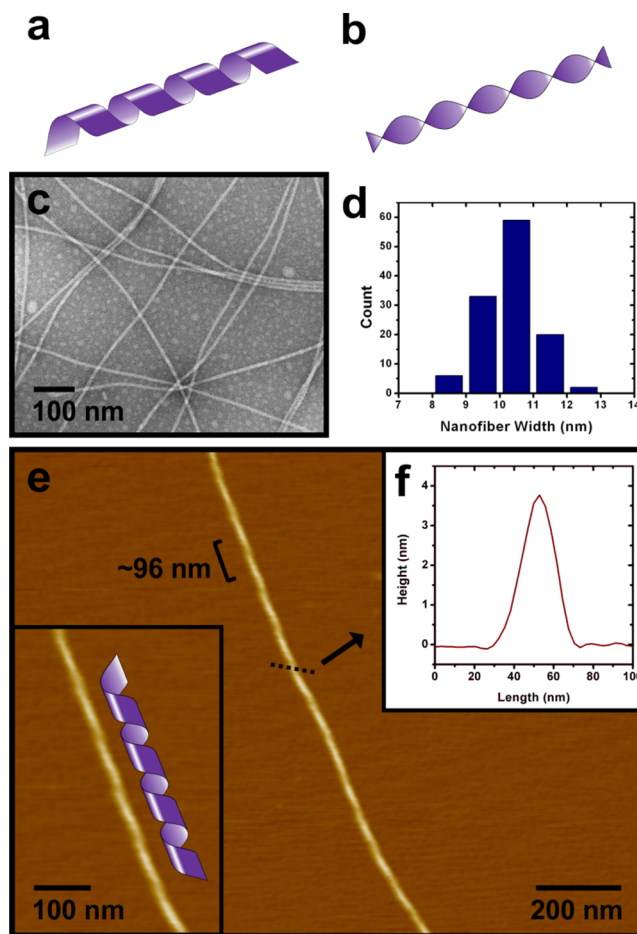

Figure 3. C_{18}-$(PEP_{Au}^{M-ox})_2$ fiber morphology studies. Helical peptide amphiphile fibers typically exhibit either (a) helical ribbon or (b) twisted ribbon morphology. (c) Negative-stained TEM image of C_{18}-$(PEP_{Au}^{M-ox})_2$ fibers. (d) Fiber widths were 10.2 ± 0.8 nm. (e) AFM reveals the helical ribbon morphology of C_{18}-$(PEP_{Au}^{M-ox})_2$ fibers with a pitch of 96.2 ± 4.8 nm and (f) a ribbon height of approximately 4 nm (height trace measured along the dashed line).

amounts, depending on the length of time allowed for the assembly process. The fiber widths, measured via TEM, are 10.2 ± 0.8 nm, which is consistent with the cryo-ET data that defined the inner diameter of the nanoparticle superstructure to be approximately 10.1 nm (*vide supra*) (Figure 3d). Morphological features of the fibers, such as their helicity, were indistinguishable using traditional TEM imaging. Tapping-mode atomic force microscopy (AFM) images clearly reveal that the fibers adopt the helical ribbon morphology (Figures 3e and S9). The pitch, measured via AFM, is 96.2 ± 4.8 nm, consistent with the pitch of the gold nanoparticle single helices. The vertical thickness of the ribbon is ∼4 nm (Figure 3f). Height traces along the fiber axis suggest that the coiled helical ribbon compresses onto the mica substrate (Figure S9e), which is not surprising as such compression/collapse is common for soft assemblies having a hollow interior.[54,55] The morphological similarities between the helical ribbons and the gold nanoparticle single helices imply similarities between the C_{18}-$(PEP_{Au}^{M-ox})_2$ assembly in both the presence and absence of gold nanoparticles. Consistent with our previous reports, these observations suggest that the geometry and structure of the peptide conjugate assembly define the nanoparticle assembly architecture. Studying and understanding the underlying

molecular structure of the C_{18}-$(PEP_{Au}^{M\text{-ox}})_2$ helical ribbons provides insights into the nature of the nanoparticle assembly and provides a basis for future studies aimed at modifying the single-helical structure.

We therefore next proceeded to examine the internal structure within the C_{18}-$(PEP_{Au}^{M\text{-ox}})_2$ fibers. An amide I absorption peak at 1630 cm^{-1}, characteristic of parallel β-sheet secondary structure,[56,57] was observed in the Fourier transform infrared (FTIR) spectrum (Figure S10). In addition, a peak at 2922 cm^{-1} corresponding to C−H stretches was observed, signifying relatively ordered packing of the alkyl chains within the assembly (Figure S10).[58] CD spectra for C_{18}-$(PEP_{Au}^{M\text{-ox}})_2$ were collected under conditions that promote fiber assembly.[59] A prominent negative band centered at ∼211 nm and a positive band centered at ∼238 nm (Figure S11a) were observed. Negative peaks corresponding to the presence of β-sheet structure are typically observed around 215−220 nm for peptide amphiphile assemblies.[60,61] We speculate that the blue-shifted negative peak could be due to the presence of multiple secondary structures within the assembly. Molecular simulation studies of PEP_{Au} predict that the proline residues near the C-terminus adopt a polyproline II (PPII) conformation when free in solution.[38] PPII helices typically display a strong negative CD band at ∼205 nm.[62,63] We observe a negative band at 205 nm for C_{18}-$(PEP_{Au}^{M\text{-ox}})_2$ under conditions that do not promote fiber assembly (i.e., no β-sheet formation; Figure S12). Therefore, we conclude that the observed signal in the CD spectrum of C_{18}-$(PEP_{Au}^{M\text{-ox}})_2$ fibers is a superposition of bands deriving from both β-sheet and PPII secondary structures in the assembled fibers.

While CD and FTIR spectroscopy provided information about the secondary structure, X-ray diffraction (XRD) experiments were conducted to probe the molecular-level packing of C_{18}-$(PEP_{Au}^{M\text{-ox}})_2$ within the fibers. XRD patterns of aligned C_{18}-$(PEP_{Au}^{M\text{-ox}})_2$ fibers displayed the prototypical pattern observed for cross-β amyloid-like structure (Figures 4 and S13).[64,65] An intense meridional reflection corresponding to a d-spacing of 4.6 Å is attributed to the H-bonding distances between peptide backbones (Figure S13b). Equatorial peaks with d-spacings of ∼6.5, ∼9, and ∼18 Å correspond to repeat

distances between β-sheets (Figures 4 and S13b). The off-meridian reflections corresponding to a d-spacing of ∼4.2 Å may be attributed to the distance between hkl planes diagonal to the planes containing the β-sheets.[66]

The CD, FTIR, and XRD data revealed that the peptide-based core of the assemblies is stabilized by substantial β-strand formation, but the location of the β-strand within the peptide is uncertain. To address this, we applied ssNMR to site-specifically labeled C_{18}-$(PEP_{Au}^{M\text{-ox}})_2$ assemblies. To probe the N-terminal end of the peptide, we applied $^{13}C,^{15}N$-labeling to the A1 residue. To probe the Pro-rich C-terminal half of the peptide, we also included in the same peptide a $^{13}C,^{15}N$-labeled P10 (Figure 5a). Figure 5b shows a 2D magic-angle spinning (MAS) ssNMR spectrum obtained for labeled C_{18}-$(PEP_{Au}^{M\text{-ox}})_2$ assemblies. The off-diagonal cross-peaks provide residue-specific assignments of each labeled residue. The P10 peaks (black dashed lines) have chemical shifts indicative of a PPII helix structure (Figure S14a).[67,68] The observation of a single set of peaks shows that P10 has the same PPII structure in all of the C_{18}-$(PEP_{Au}^{M\text{-ox}})_2$ in the sample. In contrast, A1 features multiple sets of peaks, indicating the presence of multiple structures. The dominant A1 peaks (A1a and A1b), accounting for ∼90% of the signal, have chemical shifts that indicate A1 to be part of the β-sheet structure (Figure 5c). The A1c conformer is present at much lower intensity (∼10% of the total signal), lacks β-sheet shifts, and presumably reflects peptide that failed to incorporate into the amyloid-like core (e.g., the pseudospherical aggregates observed in TEM images). In long-mixing ssNMR data, these three conformers show no sign of dynamics- or proximity-enabled polarization exchange (Figure S14b). Motion-sensitive ssNMR experiments (not shown) indicate that all sites are relatively rigid and immobilized in the peptide assemblies. Therefore, two structurally different peptide conformers, present at a 1:1 ratio, make up ∼90% of the sample (Figure 5d). The ssNMR shows that the β-sheet structure extends to the very N-terminal residue A1. At the other end, P10 is outside the β-sheet, forming instead part of a PPII helix that presumably involves much of the Pro-rich C-terminal peptide end. We note a strong analogy to our studies of fibrillar huntingtin exon 1, which also has a peak-doubled amyloid core followed by a PPII-helical Pro-rich domain.[68] In that system, the transition from the β structure to the PPII structure occurs over a single residue, making it reasonable that a similarly compact β-sheet/PPII-helix interface may occur here.

How do two equally populated β-sheet/PPII peptide building blocks (Figure 5d) coassemble into the β-sheet-based core of our assemblies? The X-ray cross-β pattern showed ∼6.5 and ∼9 Å intersheet distances between β-sheets. Sheet-to-sheet interfaces in amyloid structures have been characterized as "steric-zippers" classified into distinct symmetry classes.[69,70] The structural data, self-assembly behavior, and chemical nature of C_{18}-$(PEP_{Au}^{M\text{-ox}})_2$ point to a likely architecture of the assemblies. The C_{18} acyl tails work to bring the peptides conjugates together to form micellar structures early in the assembly process. Clustering of the C_{18} tails dictates a parallel alignment of the self-assembling peptides and thus facilitates the formation of β-sheets that are coaligned and parallel in nature. This fits well with our FTIR data and ssNMR results. Thus, these considerations restrict us to class 2 or class 3 zipper motifs.[69] Of these, only a class 3 zipper explains the doubled β-sheet ssNMR peaks and their 1:1 intensity ratio as it predicts structural differences between two
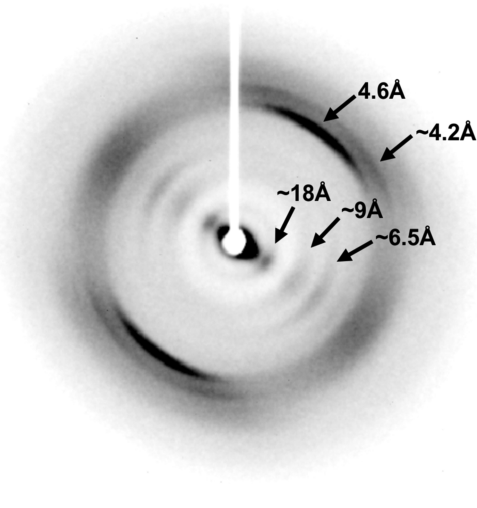

Figure 4. X-ray diffractogram. 2D X-ray diffraction pattern of aligned C_{18}-$(PEP_{Au}^{M\text{-ox}})_2$ fibers reveals a cross-β architecture. Meridional (4.6 Å), off-meridional (∼4.2 Å), and equatorial reflections (∼18, ∼9, and ∼6.5 Å) are labeled.
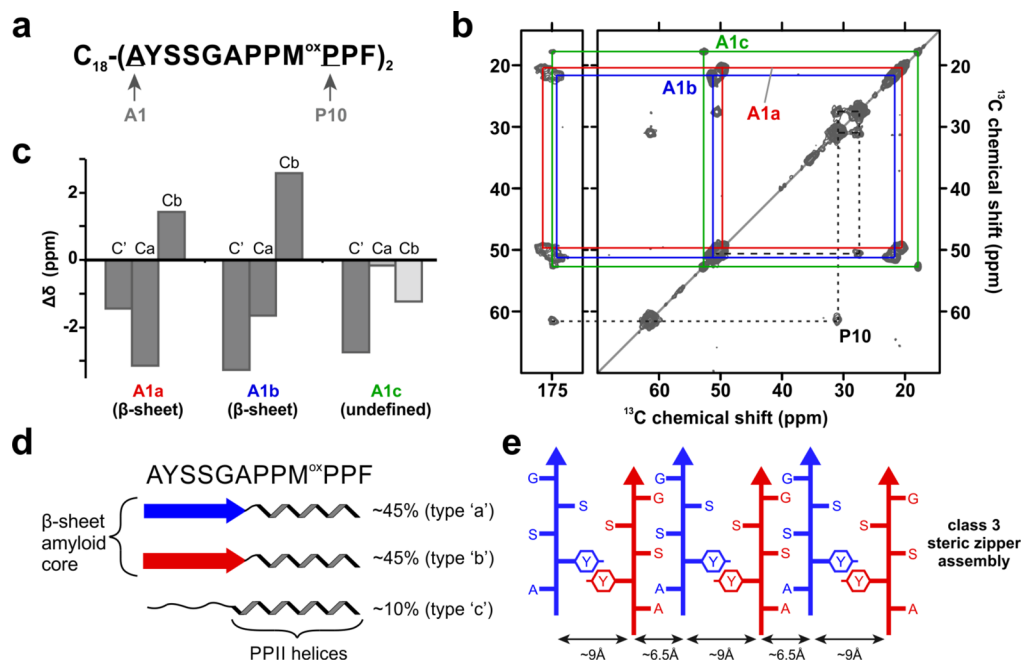
Figure 5. MAS ssNMR results. (a) Position of residue-specific ^{13}C-,^{15}N-labeling (arrows). (b) 2D ^{13}C–^{13}C MAS ssNMR of labeled C$_{18}$-(PEP$_{Au}$$^{M-ox}$)$_2$ assemblies. Dashed and colored lines connect sets of peaks from labeled P10 (black dashed line) and A1 residues (solid lines). Three A1 conformations are marked with red (A1a), blue (A1b), and green (A1c) lines. (c) Secondary structure analysis of A1 ssNMR signals, showing A1a and A1b to be part of the β-sheet core. (d) Secondary structure distribution in the three peptide conformers observed by ssNMR, along with their relative ssNMR peak intensities (right). (e) Amyloid core model based on a class 3 steric zipper architecture. The compact Ala/Ser/Gly interface and the aromatic interface present intersheet distances of ~6.5 and ~9 Å, respectively. Alternating peptides have distinct structures (blue/red coloring) that explain the observed peak doubling in the A1 β-sheet peaks.

types of coassembling β-sheets. In addition, class 3 zippers also predict the presence of two types of intersheet interfaces, which feature either odd- or even-numbered residues (Figure 5e). The odd-residue interface features only small side chains (Ala/Ser/Gly), which enable the formation of a tight intersheet interface that places the sheets ~6.5 Å apart (Figure S14c). The even-numbered interface includes the large aromatic Tyr. In amyloid-like crystal structures with parallel β-sheets, such Tyr rings adopt a characteristic ring-stacked orientation, as shown in Figure S14d. The bulkiness of the aromatic rings causes notably wide sheet-to-sheet interfaces that are ~9–10 Å apart (e.g., Figure S14e), in line with the X-ray pattern of the peptide assemblies. Thus, this kind of assembly provides an elegant rationale for the ssNMR, FTIR, and X-ray results, and it strongly argues for a peptide core structure that combines packed PPII helical C-termini with a class 3 amyloid-like assembly.

Single Helix Assembly Model. Taking into account the accumulated data on the C$_{18}$-(PEP$_{Au}$$^{M-ox}$)$_2$ assemblies, we propose a molecular packing model for the helical ribbon (Figure 6a). The ribbon consists of a monolayer of C$_{18}$-(PEP$_{Au}$$^{M-ox}$)$_2$ arranged perpendicular to the faces in a cross-β architecture. This allows the PPII helix and negatively charged carboxylates (at pH ~ 7) to be exposed on the outer surface of the helical ribbon. The model adheres to the ribbon vertical thickness constraint of ~4 nm (labeled h in Figure 6a), as measured by AFM (*vide supra*); we estimate that the peptide length is ~3.8 nm (Figure S15). Since the extended length of C$_{18}$-(PEP$_{Au}$$^{M-ox}$)$_2$ is estimated to be ~7.5 nm (Figure S15), a bilayer structure where the alkyl chains are interdigitated in the core of the ribbon would not be possible. We speculate that the aliphatic chains, which are relatively ordered (*vide supra*),

aggregate with one another at the inner surface of the helical ribbon or possibly fold inward with one another between β-sheets and therefore make only a small contribution to the measured ribbon thickness.[71] In either case, the helical ribbon architecture segregates the relatively hydrophobic N-terminus from the aqueous buffer while exposing the hydrophilic C-terminus.[72] This is in contrast to a twisted ribbon structure where both sides of the tape would be equally exposed. The ribbon width, w, is determined by the number of β-sheets stacked side-by-side with regular ~6.5 and ~9 Å distances.

On the basis of this assembly model and the structural parameters of both the single helices and C$_{18}$-(PEP$_{Au}$$^{M-ox}$)$_2$ fibers, we conclude that the gold nanoparticles decorate the outer face of the helical ribbon (Figure 6b–d). Careful inspection of the nanoparticle orientation within the super-structures (Figure 6c) indicates that the rod-like particles align in parallel along the width of the ribbons, which supports a model where particle growth proceeds in one direction (Figure 6d) and could be limited by the width of the helical ribbon. The regular distances between the particles could be due to electrostatic repulsion between particles.[24]

Since we propose that the C-termini of C$_{18}$-(PEP$_{Au}$$^{M-ox}$)$_2$ are exposed at the outer face of the helical ribbon, we reason then that the particles must be bound to the residues that make up the PPII helix. Previous reports on PEP$_{Au}$ binding onto gold surfaces conclude that Y2 and F12 bind most strongly to the 111 facets of gold nanoparticles due to their aromatic side chains.[38–40] Since the Y2 molecules are integral to the parallel β-sheet structure within the core of the peptide ribbon, the exposed phenylalanine at the C-terminus must account for much of the binding between the gold particles and the peptide assembly. In addition, methionine residues, which also bind
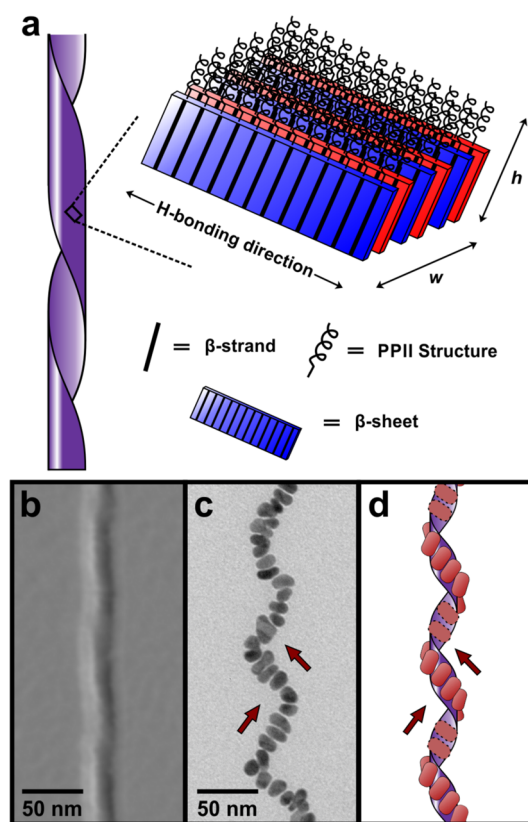
Figure 6. C_{18}-$(PEP_{Au}^{M-ox})_2$ assembly model. (a) Proposed assembly model of the helical ribbons. β-sheets run along the length of the fiber (interstrand distance = 4.6 Å). The width of the ribbon, w, is determined by the number of stacked β-sheets with lamination spacings of ~6.5 and ~9 Å. PPII helices are exposed at the outer surface of the helical ribbon. The blue and red layers correspond to the type 'a' and type 'b' β-sheets, respectively, shown in Figure 5. The aliphatic tails have been omitted for clarity. (b) AFM (amplitude image) and (c) TEM image aligned to highlight the structural similarity between the fiber assembly and nanoparticle assembly, alongside (d) the proposed single-helix assembly model with gold nanoparticles bound to the outer face of the helical ribbon. The arrows show directionality similarities of the nanoparticle orientation.

strongly, could contribute to the overall binding interaction.[40] The inner surface of the helical ribbon is sterically hindered, which prevents particle binding.

CONCLUSIONS

We have demonstrated that C_{18}-$(PEP_{Au}^{M-ox})_2$ directs the formation of well-defined single-helical gold nanoparticle assemblies having strong plasmonic chiroptical activity that ranks among the highest observed for comparable systems. In addition, we proposed a molecular assembly model based on data acquired from several characterization techniques that is consistent with the structural parameters of the single helices. This model provides foundational information for understanding how peptide conjugate molecules constructed from inorganic-binding peptides can simultaneously self-assemble and bind to inorganic nanoparticles, thus enabling the assembly of nanoparticles into intricate superstructures. Moreover, this model serves as a launching point for rigorous rational design of new peptide conjugates for directing and precisely controlling nanoparticle assembly structures and metrics. Collectively, the results presented herein underline the utility of peptide

constructs as building blocks for directing the assembly of nanoparticles into highly complex and well-defined nanoscale superstructures. Finally, they point toward future studies aimed at incorporating specific chemical modifications to the peptide side chains (e.g., oxidation, hydroxylation, phosphorylation, and glycosylation) and understanding how and why these modifications lead to morphological changes to a nanoparticle superstructure.

EXPERIMENTAL METHODS

Materials and Methods. All chemicals were purchased from either Aldrich or Fisher and used without further purification. N_3-C_4H_8CO-AYSSGAPPMPPF (N_3-PEP_{Au}) was synthesized by Pierce Biotechnology, Inc. Triethylammoniium acetate buffer (TEAA) was purchased from Aldrich (catalog number 90358) and 4-(2-hydroxyethyl)-1-piperazineethanesulfonic acid (pH 7.3) (HEPES) buffer was purchased from Fisher (catalog number BP 299-100). Chloroauric acid ($HAuCl_4$) was purchased from Aldrich (catalog number 520918). Peptide conjugates were purified using an Agilent 1200 series reverse-phase high-pressure liquid chromatography (HPLC) instrument equipped with an Agilent Zorbax 300SB-C_{18} column. Peptide conjugates were quantified based on their absorbance at 280 nm and using the extinction coefficient for tyrosine (1280 $M^{-1}cm^{-1}$). UV−vis spectra were collected using an Agilent 8453 UV−vis spectrometer equipped with deuterium and tungsten lamps. Matrix-assisted laser desorption ionization time-of-flight mass spectrometry (MALDI-TOF MS) data were collected using an Applied Biosystem Voyager System 6174 MALDI-TOF mass spectrometer (positive reflector mode; accelerating voltage: 20 kV) and using α-cyano-4-hydroxycinnamic acid (CHCA) as the ionization matrix. Nanopure water (NP H_2O, 18.1 MΩ) was obtained from a Barnstead DiamondTM water purification system.

Preparation of N_3-PEP_{Au}^{M-Ox}. N_3-PEP_{Au} (3 mg, 2.23 μmol) was dissolved in a 1:1 mixture of CH_3CN/NP H_2O. To this solution was added concentrated H_2O_2 to bring the final H_2O_2 concentration to 100 mM. The solution was vortexed and left undisturbed for 8−15 h. This final solution was purified using reverse-phase HPLC eluting with a linear gradient of 0.05% formic acid in CH_3CN and 0.1% formic acid in NP H_2O (5/95 to 95/5 over 30 min.).

Preparation of C_{18}-$(PEP_{Au}^{M-Ox})_2$. Alkyne-terminated aliphatic substrates and peptide conjugates were prepared according to protocols detailed in a previous report.[28]

Preparation of Single Helices. In a plastic vial, C_{18}-$(PEP_{Au}^{M-ox})_2$ (~18.7 nmol) was dissolved in 250 μL of 0.1 M HEPES buffer and sonicated for 5 min. After sonication, the solution was allowed to sit at room temperature for 25 min. A fresh stock solution of $HAuCl_4$ in TEAA buffer was prepared by mixing 100 μL of 0.1 M $HAuCl_4$ in NP H_2O with 100 μL of 1 M TEAA buffer. The resulting mixture was vortexed for 1 min. To the C_{18}-$(PEP_{Au}^{M-ox})_2$ solution was added 2 μL of the freshly prepared $HAuCl_4$/TEAA solution. A "dark cloud" appeared 2−4 s after the addition of the $HAuCl_4$/TEAA solution; at this point, the vial was briefly vortexed and then left undisturbed at room temperature.

Preparation of C_{18}-$(PEP_{Au}^{M-ox})_2$ Fibers. 75 μM solutions of C_{18}-$(PEP_{Au}^{M-ox})_2$ fibers were prepared in 0.1 M HEPES buffer. For CD spectroscopy studies, 10 mM HEPES buffer was used. After 1 day of sitting at room temperature, the solutions were analyzed. For some CD and TEM experiments, $CaCl_2$ was added (1 mM final concentration) to accelerate fiber formation.

Transmission Electron Microscopy. TEM images were collected with a FEI Morgagni 268 (80 kV) with an AMT side mount CCD camera system. Phosphotungstic acid (pH 7.4) was used to stain TEM sample grids for the peptide assembly studies. TEM samples were prepared by drop-casting 6 μL of solution onto a 3 mm diameter copper grid coated with Formvar. After 5 min, the excess solution was wicked away. The grid was washed with NP H_2O (6 μL) and wicked away after 1 min.

Cryogenic Electron Tomography and 3D Reconstruction. For the single-helical gold nanoparticle superstructures, 4 μL of

solution was applied to the carbon side of glow discharged perforated R2/2 Quantifoil grids (Quantifoil Micro Tools, Jena, Germany) before plunge-freezing using a manual gravity plunger. A series of images were recorded by tilting the specimen from −60 to 70° in increments of 3° (<45°) and 2° (>45°). Images were recorded on a FEI Falcon II direct electron detector camera at a nominal magnification of 39 000×. Altogether, 51 images were collected in one tilt series with a total dose of ~50 e⁻/Å². Images were recorded at a defocus value of ~0.5 μm using FEI batch tomography software. The IMOD package[73] was used to align tilted projection images and reconstruct the final 3D density map from the aligned image stack. For surface rendering, the tomogram was filtered to 20 Å resolution and displayed using the program UCSF CHIMERA.[74]

Atomic Force Microscopy. AFM images were collected with an Asylum MFP-3D atomic force microscope using tapping-mode. Images were obtained using ultrasharp AFM tips (NanoandMore, SHR-150), with a 1 Hz scanning rate. The APTES-mica was prepared by drop-casting a 0.1% APTES solution in NP H_2O onto freshly cleaved mica, and after 10 min, the mica was rinsed with NP H_2O. C_{18}-$(PEP_{Au}^{M-ox})_2$ was dissolved in 0.1 M HEPES (75 μM) and allowed to sit at room temperature overnight. After 1 day of incubation, 20 μL of the solution was drop-cast onto the APTES-functionalized mica. After 1 min, the sample was rinsed with NP H_2O and allowed to air-dry overnight.

Attenuated Total Reflectance Fourier Transform Infrared Spectroscopy. ATR-FTIR spectra were collected on a PerkinElmer Spectrum 100 FTIR instrument with a universal attenuated total reflectance sampling accessory coupled to a computer using PerkinElmer Spectrum Express software. The sample was background-corrected in air. C_{18}-$(PEP_{Au}^{M-ox})_2$ was dissolved and sonicated in 0.1 M HEPES (75 μM). After 1 day, the assembled fibers were dialyzed three times in NP H_2O using d-tube dialyzers (Millipore, catalog number 71505-3) to remove the buffer, and the fibers were concentrated. The concentrated solution containing the fibers were then drop-cast onto the ATR-FTIR substrate and allowed to air-dry.

Circular Dichroism Spectroscopy. CD measurements were conducted on an Olis DSM 17 CD spectrometer. The scan rate was 8 nm/min, and the bandwidth was 2 nm. All CD experiments were carried out in 10 mM HEPES (peptide assembly; 200−280 nm) or 0.1 M HEPES (nanoparticle assembly; 450−800 nm) with a 1 mm path length quartz cuvette at 25 °C.

Powder X-ray Diffraction. Powder X-ray diffraction was performed on a Bruker X8 Prospector Ultra diffractometer equipped with an APEX II CCD detector and an IμS microfocus Cu Kα source (λ = 1.54178 Å). The diffractograms were recorded at a distance of 15 cm at room temperature. Raw data were retrieved using the PILOT plug-in in the Bruker APEX II software package and further processed in Match! software to obtain d and intensity values. The sample was prepared by dissolving ~1.5 mg of C_{18}-$(PEP_{Au}^{M-ox})_2$ in 1 mL of 0.1 M HEPES and sonicating for 5 min. The sample was left to sit overnight. After 24 h, the solution was ultracentrifuged (r_{max} = 213 000g) for 1 h. The supernatant was removed, NP H_2O (1 mL) was added, and the sample was ultracentrifuged again at the same speed. After centrifugation, the supernatant was removed, leaving behind a clear gel. The peptide gel was loaded into a glass capillary (φ = 0.7 mm) and air-dried.

MAS Solid-State NMR Spectroscopy. Labeled N_3-PEP_{Au} was purchased from Pierce Custom Peptides, and labeled C_{18}-$(PEP_{Au}^{M-ox})_2$ was synthesized according to the protocols detailed above. Labeled C_{18}-$(PEP_{Au}^{M-ox})_2$ fibers (2 mg) were packed into thin-wall 3.2 mm zirconia MAS rotors (Bruker Biospin, Billerica, MA) by ultra-centrifugation at ~175 000g in a home-built sample packing tool spun in a Beckman Coulter Optima L-100 XP ultracentrifuge equipped with a SW-32 Ti rotor. MAS ssNMR spectra were obtained with a widebore Bruker Avance I NMR spectrometer operating at a ¹H Larmor frequency of 600 MHz (14.1 T) using a 3.2 mm HCN MAS ssNMR probe equipped with a "EFree" reduced electric field coil (Bruker Biospin). Sample temperature was maintained at 277 K using a constant flow (800 L/h) of cooled gas. Bruker Topspin software was used to acquire the spectra. Spectra were processed using NMRPipe

software and analyzed with CCPNMR/Analysis.[75,76] The ¹³C signals of adamantane were used to externally reference chemical shifts to 4,4-dimethyl-4-silapentane-1-1 sulfonic acid (DSS).[77] 1D and 2D ssNMR spectra were acquired at 10 kHz MAS, using ramped ¹H,¹³C cross-polarization (CP) with a 2.0 ms CP contact time, a 3 s recycle delay, and 83 kHz two-pulse phase-modulated (TPPM) decoupling.[78] A total of 1024 scans were obtained for the 1D CP experiment. The short-mixing ¹³C−¹³C 2D spectrum was obtained with 20 ms of dipolar assisted rotational resonance (DARR) ¹³C−¹³C mixing. The 2D spectrum in the Supporting Information features 500 ms of ¹³C−¹³C proton-driven spin diffusion (PDSD), which is expected to allow longer-range signal transfer over up to 6−7 Å.[79] Additional experimental details are summarized in Table S1 of the Supporting Information.

■ ASSOCIATED CONTENT

Ⓢ Supporting Information

The Supporting Information is available free of charge on the ACS Publications website at DOI: 10.1021/jacs.6b07322.

    LCMS, FTIR, CD, TEM, XRD, AFM, ssNMR, and additional data (PDF)

■ AUTHOR INFORMATION

Corresponding Authors
*pvdwel@pitt.edu
*nrosi@pitt.edu

Notes
The authors declare no competing financial interest.

■ ACKNOWLEDGMENTS

■ REFERENCES

(1) Fan, Z.; Govorov, A. O. *Nano Lett.* 2010, 10, 2580−2587.
(2) Govorov, A. O.; Gun'ko, Y. K.; Slocik, J. M.; Gerard, V. A.; Fan, Z. Y.; Naik, R. R. *J. Mater. Chem.* 2011, 21, 16806−16818.
(3) Guerrero-Martinez, A.; Alonso-Gomez, J. L.; Auguie, B.; Cid, M. M.; Liz-Marzan, L. M. *Nano Today* 2011, 6, 381−400.
(4) Xia, Y. H.; Zhou, Y. L.; Tang, Z. Y. *Nanoscale* 2011, 3, 1374−1382.
(5) Yang, M.; Kotov, N. A. *J. Mater. Chem.* 2011, 21, 6775−6792.
(6) Shen, X.; Song, C.; Wang, J.; Shi, D.; Wang, Z.; Liu, N.; Ding, B. *J. Am. Chem. Soc.* 2012, 134, 146−149.
(7) Kuzyk, A.; Schreiber, R.; Fan, Z.; Pardatscher, G.; Roller, E.-M.; Hogele, A.; Simmel, F. C.; Govorov, A. O.; Liedl, T. *Nature* 2012, 483, 311−314.
(8) Wang, R.-Y.; Wang, H.; Wu, X.; Ji, Y.; Wang, P.; Qu, Y.; Chung, T.-S. *Soft Matter* 2011, 7, 8370−8375.
(9) Yan, W.; Xu, L.; Xu, C.; Ma, W.; Kuang, H.; Wang, L.; Kotov, N. A. *J. Am. Chem. Soc.* 2012, 134, 15114−15121.
(10) Chen, Z.; Lan, X.; Chiu, Y.-C.; Lu, X.; Ni, W.; Gao, H.; Wang, Q. *ACS Photonics* 2015, 2, 392−397.
(11) Mastroianni, A. J.; Claridge, S. A.; Alivisatos, A. P. *J. Am. Chem. Soc.* 2009, 131, 8455−8459.
(12) Shen, X. B.; Asenjo-Garcia, A.; Liu, Q.; Jiang, Q.; de Abajo, F. J. G.; Liu, N.; Ding, B. Q. *Nano Lett.* 2013, 13, 2128−2133.

(13) Wu, X.; Xu, L.; Ma, W.; Liu, L.; Kuang, H.; Kotov, N. A.; Xu, C. *Adv. Mater.* **2016**, *28*, 5907−5915.

(14) Guerrero-Martínez, A.; Auguié, B.; Alonso-Gómez, J. L.; Džolić, Z.; Gómez-Graña, S.; Žinić, M.; Cid, M. M.; Liz-Marzán, L. M. *Angew. Chem., Int. Ed.* **2011**, *50*, 5499−5503.

(15) Lan, X.; Lu, X.; Shen, C.; Ke, Y.; Ni, W.; Wang, Q. *J. Am. Chem. Soc.* **2015**, *137*, 457−462.

(16) Jung, S. H.; Jeon, J.; Kim, H.; Jaworski, J.; Jung, J. H. *J. Am. Chem. Soc.* **2014**, *136*, 6446−6452.

(17) Yeom, J.; Yeom, B.; Chan, H.; Smith, K. W.; Dominguez-Medina, S.; Bahng; Joong, H.; Zhao, G.; Chang, W.-S.; Chang, S.-J.; Chuvilin, A.; Melnikau, D.; Rogach, A. L.; Zhang, P.; Link, S.; Král, P.; Kotov, N. A. *Nat. Mater.* **2014**, *14*, 66−72.

(18) Zhao, Y.; Belkin, M. A.; Alù, A. *Nat. Commun.* **2012**, *3*, 870.

(19) Gansel, J. K.; Thiel, M.; Rill, M. S.; Decker, M.; Bade, K.; Saile, V.; von Freymann, G.; Linden, S.; Wegener, M. *Science* **2009**, *325*, 1513−1515.

(20) Tang, L.; Li, S.; Xu, L.; Ma, W.; Kuang, H.; Wang, L.; Xu, C. *ACS Appl. Mater. Interfaces* **2015**, *7*, 12708−12712.

(21) Zhu, Y.; Xu, L.; Ma, W.; Xu, Z.; Kuang, H.; Wang, L.; Xu, C. *Chem. Commun.* **2012**, *48*, 11889−11891.

(22) Wu, X.; Xu, L.; Liu, L.; Ma, W.; Yin, H.; Kuang, H.; Wang, L.; Xu, C.; Kotov, N. A. *J. Am. Chem. Soc.* **2013**, *135*, 18629−18636.

(23) Pendry, J. B. *Science* **2004**, *306*, 1353−1355.

(24) Fu, X.; Wang, Y.; Huang, L.; Sha, Y.; Gui, L.; Lai, L.; Tang, Y. *Adv. Mater.* **2003**, *15*, 902−906.

(25) Tao, K.; Wang, J.; Li, Y.; Xia, D.; Shan, H.; Xu, H.; Lu, J. R. *Sci. Rep.* **2013**, *3*, 2565.

(26) Chen, C.-L.; Zhang, P.; Rosi, N. L. *J. Am. Chem. Soc.* **2008**, *130*, 13555−13557.

(27) Song, C.; Blaber, M. G.; Zhao, G.; Zhang, P.; Fry, H. C.; Schatz, G. C.; Rosi, N. L. *Nano Lett.* **2013**, *13*, 3256−3261.

(28) Merg, A. D.; Slocik, J.; Blaber, M. G.; Schatz, G. C.; Naik, R.; Rosi, N. L. *Langmuir* **2015**, *31*, 9492−9501.

(29) Chen, C. L.; Rosi, N. L. *J. Am. Chem. Soc.* **2010**, *132*, 6902−6903.

(30) Hwang, L.; Chen, C.-L.; Rosi, N. L. *Chem. Commun.* **2011**, *47*, 185−187.

(31) Hwang, L.; Zhao, G.; Zhang, P.; Rosi, N. L. *Small* **2011**, *7*, 1939−1942.

(32) Song, C.; Zhao, G.; Zhang, P.; Rosi, N. L. *J. Am. Chem. Soc.* **2010**, *132*, 14033−14035.

(33) Zhang, C.; Zhou, Y.; Merg, A.; Song, C.; Schatz, G. C.; Rosi, N. L. *Nanoscale* **2014**, *6*, 12328.

(34) Zhang, C.; Song, C.; Fry, H. C.; Rosi, N. L. *Chem. - Eur. J.* **2014**, *20*, 941−945.

(35) Song, C.; Wang, Y.; Rosi, N. L. *Angew. Chem., Int. Ed.* **2013**, *52*, 3993−3995.

(36) Naik, R. R.; Stringer, S. J.; Agarwal, G.; Jones, S. E.; Stone, M. O. *Nat. Mater.* **2002**, *1*, 169−172.

(37) Slocik, J. M.; Stone, M. O.; Naik, R. R. *Small* **2005**, *1*, 1048−1052.

(38) Heinz, H.; Farmer, B. L.; Pandey, R. B.; Slocik, J. M.; Patnaik, S. S.; Pachter, R.; Naik, R. R. *J. Am. Chem. Soc.* **2009**, *131*, 9704−9714.

(39) Pandey, R. B.; Heinz, H.; Feng, J.; Farmer, B. L.; Slocik, J. M.; Drummy, L. F.; Naik, R. R. *Phys. Chem. Chem. Phys.* **2009**, *11*, 1989−2001.

(40) Bedford, N. M.; Hughes, Z. E.; Tang, Z.; Li, Y.; Briggs, B. D.; Ren, Y.; Swihart, M. T.; Petkov, V. G.; Naik, R. R.; Knecht, M. R.; Walsh, T. R. *J. Am. Chem. Soc.* **2016**, *138*, 540−548.

(41) Yu, J.; Becker, M. L.; Carri, G. A. *Small* **2010**, *6*, 2242−2245.

(42) Diamanti, S.; Elsen, A.; Naik, R.; Vaia, R. *J. Phys. Chem. C* **2009**, *113*, 9993−9997.

(43) Vogt, W. *Free Radical Biol. Med.* **1995**, *18*, 93−105.

(44) Slocik, J. M.; Govorov, A. O.; Naik, R. R. *Nano Lett.* **2011**, *11*, 701−705.

(45) Yeom, B.; Zhang, H.; Zhang, H.; Park, J. I.; Kim, K.; Govorov, A. O.; Kotov, N. A. *Nano Lett.* **2013**, *13*, 5277−5283.

(46) Pashuck, E. T.; Stupp, S. I. *J. Am. Chem. Soc.* **2010**, *132*, 8819−8821.

(47) Cui, H.; Cheetham, A. G.; Pashuck, E. T.; Stupp, S. I. *J. Am. Chem. Soc.* **2014**, *136*, 12461−12468.

(48) Lin, Y.-A.; Ou, Y.-C.; Cheetham, A. G.; Cui, H. *ACS Macro Lett.* **2013**, *2*, 1088−1094.

(49) Deng, M.; Yu, D.; Hou, Y.; Wang, Y. *J. Phys. Chem. B* **2009**, *113*, 8539−8544.

(50) Uesaka, A.; Ueda, M.; Makino, A.; Imai, T.; Sugiyama, J.; Kimura, S. *Langmuir* **2014**, *30*, 1022−1028.

(51) Cui, H.; Muraoka, T.; Cheetham, A. G.; Stupp, S. I. *Nano Lett.* **2009**, *9*, 945−951.

(52) Hamley, I. W.; Dehsorkhi, A.; Castelletto, V.; Furzeland, S.; Atkins, D.; Seitsonen, J.; Ruokolainen, J. *Soft Matter* **2013**, *9*, 9290−9293.

(53) Fishwick, C. W. G.; Beevers, A. J.; Carrick, L. M.; Whitehouse, C. D.; Aggeli, A.; Boden, N. *Nano Lett.* **2003**, *3*, 1475−1479.

(54) Yang, M.; Wang, W.; Yuan, F.; Zhang, X.; Li, J.; Liang, F.; He, B.; Minch, B.; Wegner, G. *J. Am. Chem. Soc.* **2005**, *127*, 15107−15111.

(55) Albert, S. K.; Thelu, H. V. P.; Golla, M.; Krishnan, N.; Chaudhary, S.; Varghese, R. *Angew. Chem., Int. Ed.* **2014**, *53*, 8352−8357.

(56) Barth, A. *Biochim. Biophys. Acta, Bioenerg.* **2007**, *1767*, 1073−1101.

(57) Pelton, J. T.; McLean, L. R. *Anal. Biochem.* **2000**, *277*, 167−176.

(58) Jiang, H.; Guler, M. O.; Stupp, S. I. *Soft Matter* **2007**, *3*, 454−462.

(59) Stendahl, J. C.; Rao, M. S.; Guler, M. O.; Stupp, S. I. *Adv. Funct. Mater.* **2006**, *16*, 499−508.

(60) Moyer, T. J.; Cui, H.; Stupp, S. I. *J. Phys. Chem. B* **2013**, *117*, 4604−4610.

(61) Paramonov, S. E.; Jun, H.-W.; Hartgerink, J. D. *J. Am. Chem. Soc.* **2006**, *128*, 7291−7298.

(62) Zanna, N.; Milli, L.; Del Secco, B.; Tomasini, C. *Org. Lett.* **2016**, *18*, 1662−1665.

(63) Lin, Y.-J.; Chu, L.-K.; Horng, J.-C. *J. Phys. Chem. B* **2015**, *119*, 15796−15806.

(64) Serpell, L. C. *Biochim. Biophys. Acta, Mol. Basis Dis.* **2000**, *1502*, 16−30.

(65) Sunde, M.; Serpell, L. C.; Bartlam, M.; Fraser, P. E.; Pepys, M. B.; Blake, C. C. F. *J. Mol. Biol.* **1997**, *273*, 729−739.

(66) Geddes, A. J.; Parker, K. D.; Atkins, E. D. T.; Beighton, E. *J. Mol. Biol.* **1968**, *32*, 343−358.

(67) Sivanandam, V. N.; Jayaraman, M.; Hoop, C. L.; Kodali, R.; Wetzel, R.; van der Wel, P. C. A. *J. Am. Chem. Soc.* **2011**, *133*, 4558−4566.

(68) Hoop, C. L.; Lin, H.-K.; Kar, K.; Hou, Z.; Poirier, M. A.; Wetzel, R.; van der Wel, P. C. A. *Biochemistry* **2014**, *53*, 6653−6666.

(69) Sawaya, M. R.; Sambashivan, S.; Nelson, R.; Ivanova, M. I.; Sievers, S. A.; Apostol, M. I.; Thompson, M. J.; Balbirnie, M.; Wiltzius, J. J. W.; McFarlane, H. T.; Madsen, A. O.; Riekel, C.; Eisenberg, D. *Nature* **2007**, *447*, 453−457.

(70) Nielsen, J. T.; Bjerring, M.; Jeppesen, M. D.; Pedersen, R. O.; Pedersen, J. M.; Hein, K. L.; Vosegaard, T.; Skrydstrup, T.; Otzen, D. E.; Nielsen, N. C. *Angew. Chem., Int. Ed.* **2009**, *48*, 2118−2121.

(71) Ni, R.; Childers, W. S.; Hardcastle, K. I.; Mehta, A. K.; Lynn, D. G. *Angew. Chem., Int. Ed.* **2012**, *51*, 6635−6638.

(72) Aggeli, A.; Nyrkova, I. A.; Bell, M.; Harding, R.; Carrick, L.; McLeish, T. C. B.; Semenov, A. N.; Boden, N. *Proc. Natl. Acad. Sci. U. S. A.* **2001**, *98*, 11857−11862.

(73) Kremer, J. R.; Mastronarde, D. N.; McIntosh, J. R. *J. Struct. Biol.* **1996**, *116*, 71−76.

(74) Pettersen, E. F.; Goddard, T. D.; Huang, C. C.; Couch, G. S.; Greenblatt, D. M.; Meng, E. C.; Ferrin, T. E. *J. Comput. Chem.* **2004**, *25*, 1605−1612.

(75) Delaglio, F.; Grzesiek, S.; Vuister, G. W.; Zhu, G.; Pfeifer, J.; Bax, A. *J. Biomol. NMR* **1995**, *6*, 277−293.

(76) Vranken, W. F.; Boucher, W.; Stevens, T. J.; Fogh, R. H.; Pajon, A.; Llinas, M.; Ulrich, E. L.; Markley, J. L.; Ionides, J.; Laue, E. D. *Proteins: Struct., Funct., Genet.* **2005**, *59*, 687−696.

(77) Harris, R. K.; Becker, E. D.; De Menezes, S. M. C.; Granger, P.; Hoffman, R. E.; Zilm, K. W. *Magn. Reson. Chem.* **2008**, *46*, 582−598.

(78) Metz, G.; Wu, X. L.; Smith, S. O. *J. Magn. Reson., Ser. A* **1994**, *110*, 219−227.

(79) Hoop, C. L.; Lin, H.-K.; Kar, K.; Magyarfalvi, G.; Lamley, J. M.; Boatz, J. C.; Mandal, A.; Lewandowski, J. R.; Wetzel, R.; van der Wel, P. C. A. *Proc. Natl. Acad. Sci. U. S. A.* **2016**, *113*, 1546−1551.